Liquid–solid two-phase jet in a turbulent crossflow: Experiments and simulations

Charlène Octau, Talib Dbouk, Michel Watremez, Damien Méresse, Marc Lippert, Jesse Schiffler, Laurent Keirsbulck, Laurent Dubar

Version of Record: https://www.sciencedirect.com/science/article/pii/S0263876220300058
Manuscript_9bbd32e8b724521109872bbe3432e144

Liquid-solid two-phase jet in a turbulent crossflow: Experiments and simulations

C. OCTAU[b,c], T. DBOUK[a,*], M. WATREMEZ[b,c], D. MERESSE[b,c], M. LIPPERT[b,c], J. SCHIFFLER[b,c], L. KEIRSBULCK[b,c], L. DUBAR[b,c]

[a] *IMT Lille Douai, University of Lille, F-59000 Lille, France.*
[b] *LAMIH Laboratory, UMR CNRS 8201, 59300 Valenciennes, France*
[c] *Polytechnic University Hauts-de-France, 59300 Valenciennes, France*

Abstract

Compared to single-liquid and liquid-liquid jets in crossflow (JICF), liquid-solid two-phase JICF is rarely studied. An experimental setup has been developed to investigate a vertical jet of liquid-solid mixture in water turbulent crossflow at Re$\approx 2.2 \cdot 10^4$ over 4 seconds period. Rigid micro particles were injected vertically in a horizontal pure-water turbulent flow. The jet trajectory, penetration and the particles concentration were recorded via a high resolution camera with particles tracking technique. Three-dimensional CFD simulations have been conducted using two different Eulerian models: two-Fluid model in commercial code, and a new mixture model solver developed in opensource to predict the hydrodynamics, jet trajectory and particles transport. A modified-$k-\varepsilon$ model (for particle induced turbulence, and turbulent dispersion), and a modified-buoyant-$k-\varepsilon$ model have been employed in the commercial and open-source codes, respectively. At $t \leq 2.5\ s$ near the jet's entry $(x/h > 0.2,\ y/h < 0.15)$, both models predicted local ϕ values similar to the experiments. While at $t = 2.5\ s$, only the mixture model predicted the jet's bend with $\phi \approx 0$ in the zone $(x/h > 0.2,\ y/h < 0.15)$ as in the experiment. The mixture model constitutes a good compromise for conducting global predictions of suspension JICFs at a computational cost that is reduced by a factor of the order of O(~10).

Keywords: Multiphase flow, liquid-solid jet, liquid-solid mixing, particles induced turbulence, Computational Fluid Dynamics

1. Introduction

A vertical liquid-solid JICF has been rarely studied before (if never). This contribution sheds the light on this topic both experimentally and numerically.

*Corresponding author
Email address: talib.dbouk@imt-lille-douai.fr (T. DBOUK)

Nomenclature

τ	Stress Tensor [Pa]
$\mathbf{D}$	Diffusivity 2^{nd}-rank Tensor [$m^2 \cdot s^{-1}$]
$\mathbf{F}$	Force per unit volume [$kg \cdot m^{-2} \cdot s^{-2}$]
$\mathbf{g}$	Gravitational acceleration vector [$m \cdot s^{-2}$]
$\mathbf{I}$	Identity 2^{nd}-rank Tensor [-]
$\mathbf{M}$	Inter-phase momentum per unit volume [$kg \cdot m^{-2} \cdot s^{-2}$]
$\mathbf{n}$	Unit normal vector at boundary [-]
$\mathbf{T}$	Molecular Stress [Pa]
$\mathbf{U}$	Velocity vector [$m \cdot s^{-1}$]
ε	Turbulent dissipation rate [$m^2 \cdot s^{-3}$]
η	Particle eddy interaction time [$m \cdot s^{-1}$]
μ	Dynamic viscosity $Pa \cdot s$
ν	Kinematic viscosity [$m^2 \cdot s^{-1}$]
ν^t	Turbulent kinematic viscosity [$m^2 \cdot s^{-1}$]
ϕ	Volume Fraction of particles [-]
ρ	Density [$kg \cdot m^{-3}$]
σ	Turbulent Prandtl number [-]
Ξ	Particle slip velocity [$m \cdot s^{-1}$]
0	Initial or unmodified value
∞	Free stream
c	Continuous phase
d	Dispersed phase
i	Phase number [-]
m	Mean value
r	Relative value
in	Inlet
max	Maximum value
out	Outlet
A_D	Linearized drag [$kg \cdot m^{-3} \cdot s^{-1}$]
b	Ratio of continuous to dispersed acceleration terms [-]
C_D	Drag coefficient [-]
C_β	Calibration coefficient for crossing trajectories [-]
C_{VM}	Virtual mass coefficient [-]
D_h	Hydraulic diameter [m]
h	Channel's height [m]
I	Turbulence Intensity [-]
k	Turbulent kinetic energy [$m^2 \cdot s^{-2}$]
L, l	Characteristic Length [m]
N	Total number of phases [-]
n	Particles number density [-]
p	Pressure [Pa]
R	Momentum flux ratio [-]
r	Hindered settling parameter [-]
r_h	Hydraulic radius [m]
Re	Reynolds number [-]
t	Time [s]
V	Volume [m^3]
$\mathbf{T}^t$	Turbulent Stress [Pa]
CFD	Computational Fluid Dynamics
CFL	Courant-Friedrichs-Lewy law
DEM	Disctete Element Method
FVM	Finite volume Method
JICF	Jet In Cross Flow
RANS	Reynolds Averaged Navier-Stokes
TKE	Turbulent Kinetic Energy
VOF	Volume Of Fluid method

Two-phase jet in crossflow (JICF) are multiphase flows (liquid, solid and/or gas mixtures) that can be present in many natural and industrial systems such as in geophysics, chemical, industrial and process engineering (i.e. abrasive water jet cutting, pollutant dispersion, fuel injection, fluidized beds, mixers, sediments transport, etc).

These liquid-solid jet systems can be found in many chemical engineering processes (like in mixing and separation in reactors). Thus a good understanding of the

hydrodynamics, the jet trajectory and the influence of particles (interactions, induced turbulence) in liquid-solid jet systems is essential for enhancing: the overall chemical process, the design and the quality of the final products.

Both experimental and numerical studies have been conducted in the literature to investigate the mixing and the dynamics or trajectory of single-phase jet in cross flow [1, 2, 3, 4, 5, 6, 7, 8, 9, 10]. Forney et al. (1999) [8] studied numerically the single jet injection into a pipe at arbitrary angles. Torré et al. (2008) [9, 10] studied jet injection for partially baffled mixing reactors and described through CFD simulations how the jet penetrates the fluid in a stirred vessel. They constituted a general correlation for the jet trajectory and jet penetration depth as an "easy to use" correlation for research and industrial purposes. [12] studied single-phase multiple tandem jet to quantify the interactions between the different jets and the influence by the crossflow. For a detailed review about single-phase JICF, the readers may refer to [11].

Nevertheless the non-negligible amount of previous studies in the literature, most studies were limited only either to single-fluid (single liquid) or liquid-liquid jets.

Liquid-solid two-phase particle-laden JICF, has not been yet extensively investigated. The very few number of existing numerical and experimental works on liquid-solid two-phase JICF [13] require additional studies to deepen our understanding of both the particle dispersion and turbulence modeling modulation in liquid-solid multiphase flows [14] for different applications.

The present contribution will be focusing on two-phase JICF such that the jet is made of **solid-liquid binary mixture** (liquid: as continuous phase; solid particles (diameter $\geq$ 1 μm): as dispersed phase; the mixture is also known in the literature by **non-Brownian suspension**). The maximum volume fraction of particles is 6.4%. The crossflow is a turbulent flow made of pure water.

Experimental measurements on such turbulent multiphase (or non-Brownian suspension) flows are very rare, if not absent at all from the literature [15]. Many experimental studies exist in the literature but they are limited only to laminar flows of concentrated suspensions of rigid particles ([16, 17]) immersed in an incompressible liquid (Newtonian) ([18, 19, 20, 21]).

Numerical studies on laminar concentrated non-Brownian suspensions have been conducted in the literature ([22, 23, 24, 25]) for many years to understand their rheological and microstructure behaviors with different rheological applications (microparticles in liquid mixing and separation apparatus and reactors). Binary-mixture liquid-solid flows can be found in: natural sediment transport of sand in rivers and sea, soil erosion, mud slides, debris flows, iceberg formation, biological blood flow, water jet cutting, industrial slurry transportation and sewage treatment plants, etc.

Modeling *multiphase turbulent* flows is a complex task due to the locally varying *time* and *length* scales in the flow. The modeling task becomes even more complex in the case of large number of particles (which is the present case of this contribution), and it is still a topic for research and investigation. The complexity in the modeling lies in the fact that 4-way coupling technique must be employed so that the modeling to be complete, for different ratios of the particle response time τ_p to the Kolmogorov time scale τ_K, as illustrated in figure 1 by Elghobashi in 1994 [26] for different regimes. The one-way coupling regime means that particles have negligible effect on turbulence. In other words, it means that particle dispersion depends on the state of turbulence of the

continuous phase, due to very low particles concentration (the particles to turbulence momentum transfer posses insignificant effect on the flow). The two-ways coupling regime means that momentum transfer from the particles is large enough to modify the local turbulence structures (e.g. an increase in the turbulence energy dissipation rate, or enhanced production of turbulence energy depending on the particles diameter). The four-way coupling regime dense suspensions) means that in addition to the two-way coupling between the particles and turbulence, particle-particle collision/interactions takes place.

Modeling of turbulent multiphase flows in CFD might be achieved, at an accepted accuracy level versus acceptable computational cost, depending on the modeling approach that is adopted [27, 26]. For example, Figure 2 lists the different modeling approaches that can be applied in computational Fluid Dynamics showing the increase of accuracy on the trade of an increase in the computational cost. The most computationally expensive approach is the DEM-CFD Euler-Lagrange approach that resolve for the dynamics of fluid, each particle and the particles-particles contacts [28, 29].

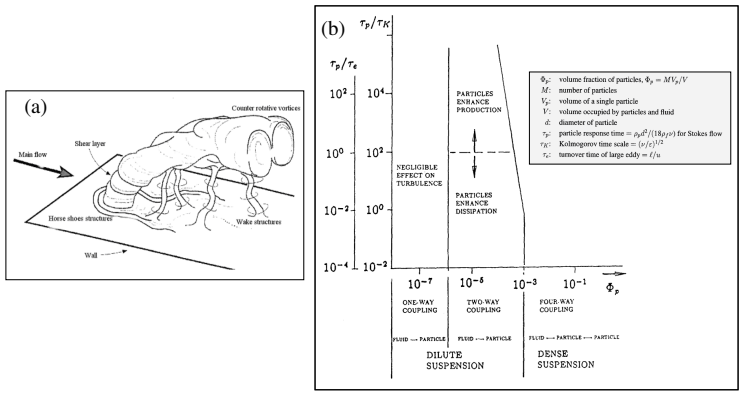

Figure 1: (a) The vortical structures of a jet in a crossflow, adopted from Fric and Roshko [31]. (b) Map of regimes of interaction between particles-in-fluid and turbulence, reproduced from [26].

Traditional multiphase CFD codes include usually RANS-turbulence models that predict turbulence thanks to a homogenization approach. Applying these traditional RANS multiphase models, based on many averaging techniques, works well on specific cases (like in homogeneous distribution or slight change of concentrations, and for some type of particles or bubbles (dispersed phase)). In traditional CFD, the numerical parameters behind the models are usually adjusted based on experimental measurements conducted on specific systems (liquid-gas, or solid-gas systems). But when it comes to dispersed solid particles (in a turbulent liquid flow as continuous phase), to the authors knowledge there is no yet enough experimental detailed characterization of these complex solids-liquid systems. Thus the RANS models must be adjusted numerically in order to take into account the observed experimental phenomena for example by employing 4-ways coupling techniques to account for: particles-particles, particles-fluid and fluids-particle interactions, and the local induced turbulence.

As shown in figure 2, the advantage of the Euler-Euler Approach lies in the small

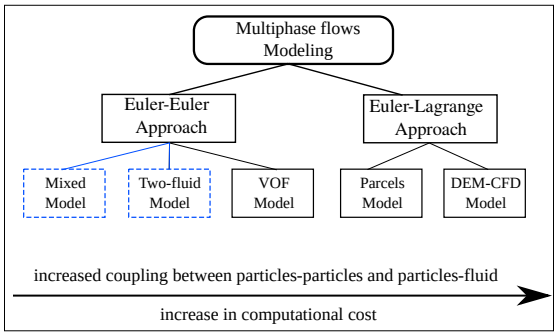

Figure 2: Multiphase flows modeling approaches. DEM: Descrete element method; VOF: Volume of fluid. A focus in this manuscript is given to the Euler-Euler approach where a mixture model and a two-fluid Model are applied.

computational cost. Its disadvantage lies in the validity-limit of the applied correlations or models. For example, a certain drag coefficient correlation model (or a RANS turbulence model) might work well for a specific range of local volume fraction values, Reynolds numbers, immersed-particles properties. But this same model must be adjusted or totally reconstructed to handle correctly different situations when the flow conditions or system properties might change (i.e. modified particles, polydispersity, rigidity, subsonic, supersonic flows, etc.).

As explained by Elghobashi 1994 [26], it is very challenging to model and predicting turbulent multiphase (particles-in-fluid) flow behavior due to the following :

- The presence of a very wide spectrum of important *length and time scales* which are associated with the dispersed phase microscopic physics and both the fine and large structures of turbulence.
- The resolution of the disparate scales that must be conducted at the particle's smallest scale motions to be highly accurate, that can be then extrapolated into numerical simulations at larger scales.
- Despite the numerous efforts, the physics of turbulence remains incomplete (e.g. lack of universality) of the current mathematical models of turbulence.

The objectives from the numerical part are to investigate the bend of the liquid-solid jet, particles transport and the overall computational costs, employing both:

- A two-fluid model in commercial CFD code,
- A newly developed mixture model in opensource CFD code.

2. Experimental measurements

The experimental measurements presented in this section, consist of the acquisition of pairs of images at high frequency in order to follow the particles dynamics and determine their concentration field using image post-processing techniques.

2.1. Experimental setup

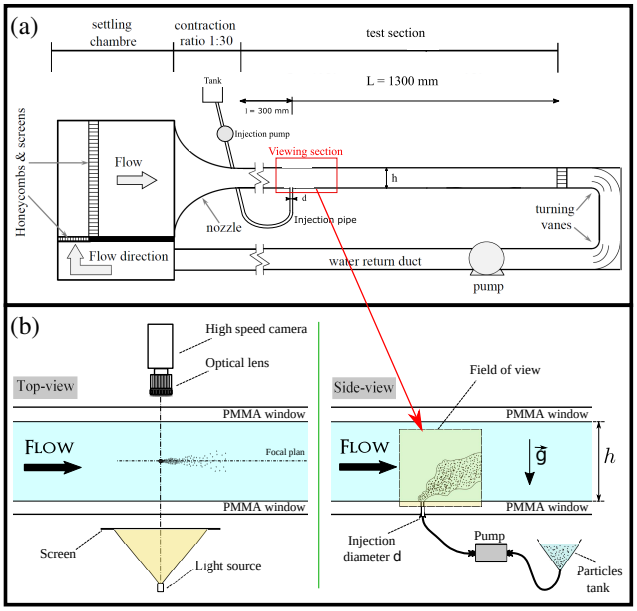

Figure 3: (a) Hydrodynamic channel description and apparatus. (b) Sketch of the shadowgraphy technique applied to the field of view.

A closed-loop hydrodynamic channel with a squared test section of a height, h of 150 mm and 1300 mm long (see figure 3-a) is used for the conducted experiments. This channel was designed to operate at low speeds and is able to generate a stable flow in time and homogeneous in space, even for very low speeds. It is equipped with a DC motor with a power of 2.2 kW which drives, by mean of a belt transmission, a pump placed in the return duct, as shown in figure 3-a. The maximum flow rate achieved in the test section is of 1.5 m/s. In order to set the injection of the particles (via a pump), and to take into account the effects of the gravity on their transport, a hole was made, with a diameter $d = 6.4$ mm on the lower plate of the test section, at 300 mm from the inlet, allowing the flow to reach stable conditions.

The used camera, is a 1 mega-pixel high speed camera (Phantom Miro 310) with a maximum acquisition rate of 3200 frames-per-second (fps) at full resolution (1280×800). The measurements are carried out with a frame rate of 1000 fps at full resolution to prevent streaking effect due to the particle motion during the acquisition. The optics used had a focal length of 85 mm, placed at 300 mm from the injection hole and with an aperture of f/5-6 (giving a field depth of 3 mm), in order to have a suitable particles jet field of view ($\Delta x/h \approx 0.6$ and $\Delta y/h \approx 0.35$). The minimum digital exposure is $1\mu s$.

2.2. Materials used

Molybdenum particles powder, with a density of about 10.22 g/cm^3, were used for the injection. The particle size distribution of is typically skewed because a large

portion of particles are formed from the breakup of larger particles into smaller ones. The peculiarity and complexity of this powder is of great interest in industry where its transport is important to understand. The granulometry analysis is obtained by using a Micrometrics Mastersizer 3000 granulometer with HydroEV module. It exhibits a particles-by-count peak of $7\mu m$ and a mean value around $20\mu m$.

Observations of the particles' shape have been carried out by means of a JEOL JSM-7100F TTLS scanning electron microscope. Most of the particles do not seem too elongate and almost exhibit a spherical mean shape.

2.3. Experimental techniques

The shadowgraphy technique is used here to obtain an estimation of the particle concentration fields. Those concentration fields are computed from each image acquired, by using the pixel intensity level which is determined by taking into consideration a reference of concentration level at the injection output. The principle of shadowgraphy is to light up a screen with a light source in order to provide a sharp contrast between the particles of interest and the background as shown in the filed of view of figure 3. The particles of interest are located between the background and the camera, and the resulting images consist of particles shadows.

The intensity value is correlated to the volume fraction of particles as the following: a maximum intensity value is considered corresponding to a maximum concentration or volume fraction of particles. For the liquid-particles mixture jet depth, it was quantified experimentally after correlating the local intensity level to the local concentration at the inlet (from images taken in a plane in the direction parallel to the jets direction). In other words, the local concentrations (volume fraction inlet boundary condition) were obtained as function of the local intensity level. For the experimental reproducibility verification, the same experimental measurement was repeated tens of times, where the same behavior is observed thus confirming the reproducibility validity (acquisition) of the experimental data results.

2.4. Post-processing of experimental data

The experiments have a duration of 4 s starting with the injection until all the liquid-solid mixture is injected and dispersed out of the field of view. During the experiment, the horizontal flow was set at a constant velocity of 0.15 m/s and the particles injection velocity was set at 0.95 m/s. Those values were defined only to allow getting a sufficiently good visualization for image post-processing. The main objective of the experiment is to validate the potential of an Euler-Euler modeling approach with a modified-$k-\varepsilon$ turbulence model to predict correctly the complex physical phenomena observed experimentally. The data processing was done using Matlab software. As presented earlier, the post-processing consists of computing the concentration fields by using the pixel intensity levels of each image obtained. This reference concentration is taken at the exit of the injection hole where the concentration is supposed to be the most important. This maximum value is then considered as equal to 1 and the gray level ratio between the gray level associated with this maximum value and the others, makes it possible to obtain an estimated concentration of particles C^*. Moreover, in order to suppress the background and unwanted fluctuations, a reference image has

been subtracted from all the images recorded by the high speed camera. It is considered that at a high gray level (reference concentration for example) in the pixel, the particle concentration is maximum, and for a low gray level (white), the concentration is minimum. A similar methodology for the determination of concentration field has been used by Cierco et al. [30] in the case of aeolian transport of sand in a steady flow.

In order to be compared with numerical data, the experimental snapshots are slightly time-averaged around the instantaneous time t (using a moving average method) and smoothed to avoid any artificial discrepancy due to optical artifacts and to eliminate the small random vortices on the jet.

The experimental case studied here is defined as a flow field were a jet of liquid-solid particles mixture enters and interacts with a turbulent crossflow of pure water at Re$\approx 2.2 \cdot 10^4$. As the crossflow passes, the jet bends in the direction of the crossflow, as shown in the figure 1-a. Former research [31] has shown that the development of the jet trajectory is dependent on the momentum flux ratio R and the Reynolds number Re_{jet} of the jet, as the following:

$$R = \sqrt{\frac{\rho_{jet} U_{jet}^2}{\rho_f U_f^2}} \tag{1}$$

$$Re_{jet} = \frac{U_{jet} L_{jet}}{\nu_{jet}} \tag{2}$$

where U_{jet}, and U_f are respectively, the velocities of the jet and the crossflow. ρ_{jet}, and ρ_f are respectively, the densities of the jet and crossflow and L_{jet} the characteristic length of the jet.

In the case of low momentum ratios, the jet will bend directly above the exit, whereas for high momentum ratios the jet trajectory will penetrate higher in the crossflow before it bends. Most of the injection in the present work is made at high momentum ratio ($R > 3$). In addition, the interaction between the jet and the horizontal flow in the channel results in a complex flow field consisting of several vortex structures such as Leading edge and lee-side vortices along the jet, horseshoe vortex system near the exit, wake vortices and counter-rotating vortex pair, as shown in figure 1-a adopted from Fric et al. [31]. Those structures have been well observed during the acquisition of the images. They contribute to the dispersion of the particles in the main flow as we move away from the exit of the jet.

3. Numerical modeling and simulations

The following two approaches based on Euler-Euler modeling approach have been employed and investigated in the present work to represent the dynamics of the liquid-solid JICF (see figure 2):

- the Euler Euler two-fluid Model (using the commercial CFD package Star-CCM+)
- the mixture Model (a new solver has been developed in the open-source CFD package OpenFOAM)

Additionally, two modified RANS turbulence models have been employed:

- a modified $k-\varepsilon$ model to account for particles-induced turbulence (in Star-CCM+)
- a buoyant $k-\varepsilon$ model that accounts for density contrasts due to concentration contrast and the influence on turbulence modularity (in OpenFOAM)

3.1. The Mixture Model

A mixture model approach has been applied in the open source OpenFOAM CFD platform. A new solver has been developed in OpenFOAM by deriving a drift flux model from the two-fluid Model equations to account for:

- Liquid-solid mixture (or non-colloidal suspension) flow rheology
- Drift-flux approximation for the relative motion of the two phases
- Buoyant-$k-\varepsilon$ RANS turbulence model

3.1.1. Mixture Continuity Equation

Using the following two constitutive relations:

$$\rho_m = \phi_c \rho_c + \phi_d \rho_d \tag{3}$$

and

$$\rho_m \mathbf{U}_m = \phi_c \rho_c \mathbf{U}_c + \phi_d \rho_d \mathbf{U}_d \tag{4}$$

inside the equation (13), the continuity equation of the mixture Model (see [32]) can be derived as the following:

$$\frac{\partial (\rho_m)}{\partial t} \; + \; \nabla \cdot (\rho_m \mathbf{U}_m) \; = 0 \tag{5}$$

3.1.2. Mixture Momentum Equation

The momentum equation of the mixture [32] is given as:

$$\frac{\partial \rho_m \mathbf{U}_m}{\partial t} + \nabla \cdot (\rho_m \mathbf{U}_m \mathbf{U}_m) = -\nabla p_m + \nabla \cdot \left(\tau + \tau_t - \tau_{diff}\right) + \rho_m \mathbf{g} \tag{6}$$

3.1.3. Mixture Diffusion Stress Tensor

The momentum diffusion due to the relative motion between the two phases is represented by a diffusion stress τ_{diff} given as the following:

$$\tau_{diff} \; = \; \sum_{k=[c,d]} \phi_k \rho_k \mathbf{U}_{km} \mathbf{U}_{km} \tag{7}$$

where $\mathbf{U}_{km} = \mathbf{U}_k - \mathbf{U}_m$ is the phase "k" velocity with respect to the mixture's center of mass (or diffusion velocity of the phase "k").

Following Ishii and Hibiki [33], one can write:

$$\phi_c \rho_c \mathbf{U}_{cm} + \phi_d \rho_d \mathbf{U}_{dm} = \mathbf{0} \tag{8}$$

and the diffusion stress can be then written as the following:

$$\tau_{diff} = \rho_m \frac{\phi_d}{\phi_c} \frac{\rho_d}{\rho_c} \mathbf{U}_{dm}^2 \tag{9}$$

3.1.4. Relative Diffusion Velocity Modeling

In the case of two-phase flows, Ishii and Hibiki [33] states that drag correlations should be expressed in terms of the drift velocity $\mathbf{U}_{dj}$. For that, the relative diffusion velocity $\mathbf{U}_{dm}$is expressed as function of $\mathbf{U}_{dj}$ as the following:

$$\mathbf{U}_{dm} = \frac{\rho_c}{\rho_m} \mathbf{U}_{dj} \tag{10}$$

The drift velocity $\mathbf{U}_{dj}$ represents the terminal velocity such that for particles of non-uniform size, [34], 3 regimes can be identified:

- Solids in suspension which don't settle due to their loose aggregate structure (i.e. concentration of a few mg/l).
- Highly settling solids with concentrations between 100-500 mg/l.
- Slowly settling solids with concentrations greater than 500 mg/l.

Categorizing suspended solids concentration in this way leads the following double exponential law:

$$\mathbf{U}_{dj} = \mathbf{U}_0 \left(e^{-r_h \phi_d} - e^{-r_p \phi_d} \right) \tag{11}$$

r_h is the settling parameter for hindered settling, r_p the settling parameter for low solid concentrations and $\mathbf{U}_0$ the effective maximum settling velocity.

3.1.5. Mixture Viscosity Model

A mixture viscosity model is applied based on non-colloidal suspension flow of rigid particles as the following:

$$\mu_m = \mu_c \left(1 - \frac{\phi_m}{\phi_{max}} \right)^{-2} \tag{12}$$

The above expression (equation 12) is derived from rheometry measurements conducted on non-colloidal suspension flows [35], where $\phi_{max} = 0.71$ represents the maximum packing volume fraction of particles of non-uniform size (or polydispersed particles).

3.1.6. Turbulence Modeling

Buoyancy-affected flow behavior (Gravity effects) due to a large density ratio that induces local variations in particles concentration is present where ($\frac{\rho_p}{\rho_l} = 10.3$) with the flow regime being turbulent. Thus buoyancy forces have an important influence on the production and dissipation of the turbulent kinetic energy (TKE). In order to account for this influence and enhance the accuracy of turbulence prediction in such situation, a modified buoyant-$k-\varepsilon$ model is applied based on the works by [36, 37]. This modified model is implemented based on an additional buoyancy generation/dissipation term applied to the k and ε equations of the standard $k-\varepsilon$ model [36, 38]. The implementation is based on the density rather than temperature-gradient extending the applicability to systems in which the density-gradient may be generated by variation of concentration of particles rather than temperature. A detailed description of this specific buoyant $k-\varepsilon$ turbulence model can be found in [36].

3.2. The Two-Fluid Model

The two-fluid Model is computationally more expensive than the mixture Model as it was illustrated in figure 2. The isothermal two-fluid model [27] will be described in this section (as general description for multiphase flows) as described in the commercial software Siemens Star-CCM+, intended to simulate the vertical liquid-solid JICF. The main objective is to investigate the potential of the two-fluid model in commercial CFD code, with a modified-$(k-\varepsilon)$ RANS turbulence model, to predict (at which accuracy compared to the mixture Model new solver in OpenFOAM ? and at which computational cost ?) the liquid-solid jet's bend as observed experimentally.

3.2.1. Continuity and momentum equations

Under a two-fluid model description, the conservation of mass for a generic phase i is given as the following:

$$\frac{\partial\left(\phi_i \rho_i\right)}{\partial t} + \nabla \cdot \left(\phi_i \rho_i \mathbf{U}_i\right) = 0 \tag{13}$$

where ϕ_i is the volume fraction of the phase i of volume V_i that satisfies:

$$\sum_{i=1}^{N} \phi_i = 1 \;\; ; \;\; V_i = \int_V \phi_i \, dV \tag{14}$$

ρ_i the density, $\mathbf{U}_i$ the velocity vector and N the total number of phases ($N = 2$ if only one continuous phase and one dispersed phase are considered, as in the present contribution).

The particles number density n of particles of spherical effective shape, immersed in a total volume V, can be estimated as the following:

$$n = \frac{3\phi_i}{4\pi {r_h}^3} V \tag{15}$$

where r_h denotes the hydraulic radius of a solid particle dispersed in the continuous phase (fluid).

The momentum equation of an Eulerian multiphase flow is given as the following:

$$\begin{aligned}\frac{\partial(\phi_i\rho_i\mathbf{U}_i)}{\partial t} \;+\; \nabla\cdot(\phi_i\rho_i\mathbf{U}_i\otimes\mathbf{U}_i) \;&=\; -\,\phi_i\nabla p \;+\; \phi_i\rho_i\mathbf{g} \\ &+\; \nabla\cdot[\phi_i(\mathbf{T}_i+\mathbf{T}_i^t)]+\mathbf{M}_i \;+\; (\mathbf{F}_{inter})_i\end{aligned} \tag{16}$$

Where p denotes the pressure field, $\mathbf{g}$ the gravitational force vector, $\mathbf{M}_i$ the inter-phase momentum transfer per unit volume, $\mathbf{T}_i$ and $\mathbf{T}_i^t$ the molecular and turbulent stresses and $\mathbf{F}_{inter}$ are internal forces such as the solid-pressure force between particles (or granular stress).

The inter-phase momentum transfer represents the sum of all the forces $\mathbf{F}_{ij}$ the phases exert on one another as it will be shown next, and satisfies the following equation:

$$\sum_{i=1}^{N}\mathbf{M}_i = 0 \tag{17}$$

3.2.2. Multiphase interaction laws

In a general modeling description, the continuous-dispersed phase interactions are represented via several forces per unit volume in the momentum transfer term $\mathbf{M}_i$ of equation (16) as the following:

$$\mathbf{M}_i = \sum_{j\neq i}\left(\mathbf{F}_{ij}^{D} \;+\; \mathbf{F}_{ij}^{L} \;+\; \mathbf{F}_{ij}^{VM} \;+\; \mathbf{F}_{ij}^{TD} \;+\; \mathbf{F}_{ij}^{WL}\right) \tag{18}$$

The subscripts: D, L, VM, TD and WL in the force terms, represent: drag, lift, virtual-mass, turbulent dispersion and wall-lubrication forces, respectively.

In the present manuscript, external sources terms, wall-lubrication, lift and virtual-mass forces will be assumed very small (thus negligible) compared to drag and turbulent dispersion forces.

The subscript ij represents a force, on phase i, due to phase j while the force per cell volume, on phase j, due to phase i is given by:

$$\mathbf{F}_{ji} = -\mathbf{F}_{ij} \tag{19}$$

3.2.3. Drag force

The force acting on a dispersed phase j due to the drag of phase i is given by:

$$\mathbf{F}_{ij}^{D} \;=\; A_D\mathbf{U}_r \quad ; \quad \mathbf{U}_r = \mathbf{U}_j - \mathbf{U}_i \tag{20}$$

where $\mathbf{U}_r$ is the inter-phase relative velocity and A_D is a linearized drag as a function of C_D which is the drag coefficient of particles. The Gidaspow Drag Model [39, 40] is applied since it is usually appropriate for dense solid dispersed-phase applications. It is based on an extended Ergun equation (or Darcy-Forchheimer) model for regions of high particle concentrations, and a modified Stokes law for regions of low particle concentrations. It is given as the following:

$$A_D = \begin{cases} \frac{150{\phi_d}^2\mu_c}{\phi_c l_{cd}^2} + \frac{1.75\phi_d\rho_c|\mathbf{U_r}|}{l_{cd}} & if \quad \phi_d \geq \phi_{tr} \\ \frac{3}{4}C_D\frac{\phi_d\rho_c}{l_{cd}}|\mathbf{U}_r|{\phi_c}^n & if \quad \phi_d < \phi_{tr} \end{cases} \tag{21}$$

where l_{cd} is an interaction length scale between the continuous and dispersed phases that is set usually to the scale of an averaged particles diameter. ϕ_d and ϕ_c are the respective concentrations of the dispersed and continuous phases. ϕ_{tr} is a transition concentration parameter to be defined by the user depending on the type of application and to the high and/or low loading of particles (ϕ_{tr} was set equal to ϕ_{max} in the present work). n is a constant parameter set by default to -1.65, and ρ_c is the density of the continuous phase.

The origins of the Gidaspow model goes back to the works by Wen and Yu 1966, known also in the literature by the "Wen-Yu-drag-model" [41].

C_D is the drag coefficient that can be measured, and then correlated by a numerical model as a function of the dispersed phase Reynolds number Re_d as it will be explained next (see [42, 43]).

For the drag coefficient C_D, in the present contribution, the Schiller-Naumann model has been applied as a correlation drag coefficient model [42], for rigid spherical particles immersed in a Newtonian fluid. It is given as the following:

$$C_D = \begin{cases} \frac{24}{Re_d}\left(1 + 0.15\,{Re_d}^{0.687}\right) & if \;\; 0 < Re_d \leq 1000 \\ 0.44 & if \quad Re_d > 1000 \end{cases} \tag{22}$$

with Re_d is the effective Reynolds number given by:

$$Re_d = \frac{\rho_c|\mathbf{U}_r|d_{eff}}{\mu_c} \tag{23}$$

where μ_c is the dynamic viscosity of the continuous phase, and d_{eff} is the particles effective diameter.

It is important to note that several C_D drag coefficient models exist in the literature depending on the volume fraction, geometry and type of application (droplets in gas or liquid, solid particles in gas or liquid, etc). Furthermore, CFD commercial and open source codes **implement differently** *similarly-named drag coefficient models* (e.g. see Greifzu et al. 2016 [44]).

Due to the fact that there is no access to modify directly the C_D value inside the commercial software Siemens Star-CCM+ library, the Gidaspow drag model paremeters n and l_{cd}" were modified instead. This is to investigate the influence of increasing the drag coefficient A_D on the results employing the Gidaspow fluid-solid drag coefficient model in the two-fluid approach (see equations 21 and 22).

Varying "n" between -1 and -10 resulted in no influence on the results because the continuous-phase volume fraction ϕ_c has values that vary between 0.94 and 1. Thus resulting in no big effect of the term $C_D\phi_c^n$ in equation 21. The value of "n" inside Star-CCM+ is set by default to -1.65.

However, varying the characteristic interaction length "l_{cd}" between 5 μm and 20 μm, resulted in an more important effect on the results. Thus a big effect of the

terms $\frac{\phi_d}{l_{cd}}$ and $\frac{C_D}{l_{cd}}$ in equation 21.

3.2.4. Turbulent Modeling

A modified $k-\varepsilon$ RANS turbulence model is applied where its description can be found in details in the Appendix.

The turbulent dispersion force $\mathbf{F}_{ij}^{TD}$ is introduced in the momentum transfer (equation 16) to take into account the influence of turbulence on the redistribution of non-uniformities in phase concentration as the following:

$$\mathbf{F}_{ij}^{TD} \;=\; A_D\,\mathbf{U}^{TD} \tag{24}$$

where $\mathbf{U}^{TD}$ is a relative drift velocity due to the application of volume-fraction weighted definitions of phase velocity, that can be written as:

$$\mathbf{U}^{TD} \;=\; \mathbf{D}_{TD}\cdot\{\nabla\ln(\phi_d)-\nabla\ln(\phi_c)\} \tag{25}$$

$\mathbf{D}_{TD}$ is a tensor diffusivity coefficient that is approximated isotropically from the continuous phase turbulent diffusivity such that:

$$\mathbf{D}_{TD} \;=\; C_0\frac{\nu_c^t}{\sigma_\phi}\mathbf{I} \tag{26}$$

where $\mathbf{I}$ is the identity matrix, ν_c^t the turbulent kinematic viscosity of the continuous phase, C_0 a parametric constant usually set to unity. σ_ϕ is the turbulent Prandtl number for volume fraction ϕ represented by Thai-Van et al. [45] model for the effective turbulent diffusivity of particles based on Simonin's analysis [46] of particle behavior in steady homogeneous turbulence. It is given by the following:

$$\sigma_\phi \;=\; \sigma_0\sqrt{1+C_\beta\Xi^2}\left(\frac{1+\eta}{b+\eta}\right) \tag{27}$$

where σ_0 is the unmodified Turbulent Prandtl number, assumed to be unity to represent basic passive diffusivity, C_β a calibration coefficient to account for crossing-trajectories effect and Ξ is the particle slip velocity scaled by the turbulent fluctuation velocity $\mathbf{U}'$.

η is the particle-eddy interaction time, scaled by particle relaxation time and b is the ratio of the coefficients of the continuous/disperse acceleration terms in the equation of motion for a particle given by Tchen's closures theory [45] as the following:

$$b \;=\; \frac{1+C_{VM}}{\frac{\rho_d}{\rho_c}+C_{VM}} \tag{28}$$

C_{VM} is the virtual mass coefficient that depends on the continuous phase volume fraction ϕ_c, such that:

$$C_{VM} \;=\; \begin{cases} 0.5 & if\;\; 0.5\le\phi_c\le 1 \\ 0 & if\;\; 0\le\phi_c<0.5 \end{cases} \tag{29}$$

3.3. Geometry, mesh and boundary conditions

The geometry of the three dimensional channel is presented in figure 4-a. The boundary conditions of velocity, pressure and volume fraction of particles were imposed as the following:

$$\begin{cases} inlet\ no.1: \ U_x = U_{1in} = 0.15\ m\ s^{-1} \quad ; \quad \phi = \phi_{1in} = 0;\ \nabla p \cdot \mathbf{n} = 0 \\ inlet\ no.2: \ U_y = U_{2in} = 0.95\ m\ s^{-1} \quad if\ \ t < 2.5\ s\ with \\ \ \ U_{2in} = 0 \quad if\ \ t \geq 2.5\ s; \quad \phi = \phi_{2in} = \phi^*(t);\ \nabla p \cdot \mathbf{n} = 0 \\ walls: \ \mathbf{U}(U_x;\ U_y;\ U_z) = (0;\ 0;\ 0);\ \nabla p \cdot \mathbf{n} = 0 \\ outlet: \ p = p_{out} = 0;\ \nabla \mathbf{U} \cdot \mathbf{n} = \mathbf{0} \end{cases} \tag{30}$$

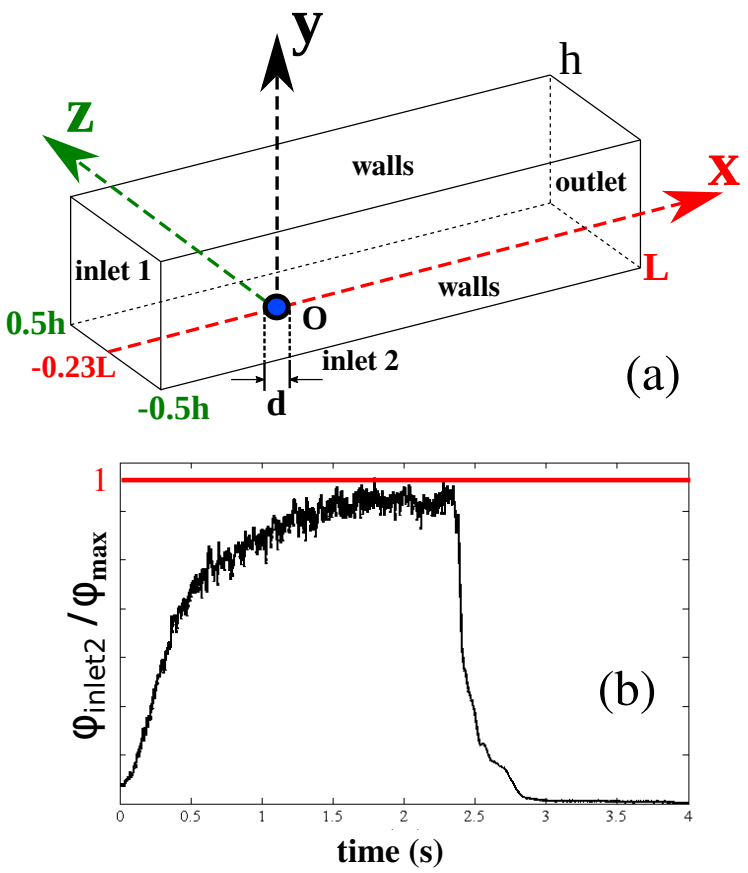

Figure 4: (a) The geometry of the 3D channel and the applied boundary conditions. (b) Volume fraction $\phi^*(t)$ boundary condition, as measured experimentally, is imposed at the vertical injection inlet2 ($\phi_{max} = 6.4\%$).

The velocity boundary conditions were considered uniform at the two inlets, based on the averaged values imposed by the injection pumps shown in figure 3. A nozzle of length zero was applied numerically based on the fact that the velocity and the paricles

volume fraction were both measured at this position (inlet at y=0), and their experimental data profiles were inject numerically as boundary condition ($\phi^*(t)$ of figure 4-b). The thermal boundary conditions have been well controlled in the experimental setup by measuring the temperature in the room, and it was assumed isothermal because the period of a single experimental data acquisition never exceeded 4 seconds in total (thus over a very short period of time, see figure 4-b).

The volume fraction boundary condition injected at the vertical entry is imposed from experimental measurements as a function of time $\phi^*(t)$ as it is illustrated in figure 4-b.

The boundary conditions for the turbulent kinematic energy (TKE) k and its dissipation rate ε are estimated as function of the turbulence intensity I derived from the equilibrium turbulent flow [47] as the following:

$$k = \frac{3}{2}(U_\infty I)^2 \tag{31}$$

$$\varepsilon = \frac{C_\mu^{\frac{3}{4}} k^{\frac{3}{2}}}{l} \tag{32}$$

with

$$I = 0.16 Re^{-\frac{1}{8}} \;\; ; \;\; l = 0.07 D_h \tag{33}$$

U_∞ is free stream flow velocity, and D_h is the hydraulic diameter.

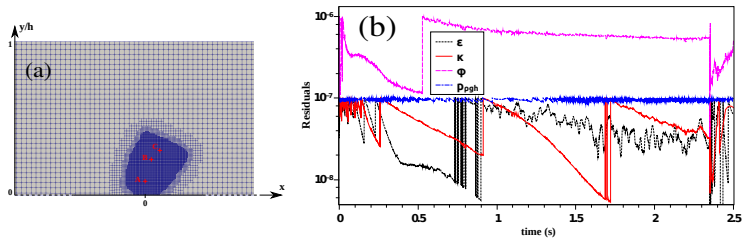

Figure 5: (a) Mesh refinement near the jet entry showing the local points A ($x/h = 0$, $y/h = 0.1$), B ($x/h = 0.05$, $y/h = 0.25$) and C ($x/h = 0.1$, $y/h = 0.3$) for the adopted mesh of 2.16 million cells. (b) An example of the residuals as function of time between 0 and 2.5 seconds using the new solver mixture model in OpenFOAM.

The numerical method employed to descretize and solve all the equations is the Finite Volume Method (FVM). A non-uniform structured mesh (or grid) has been generated and applied with local refinement near the entry of the vertical jet as shown in figure 5-a. A second order scheme was used in space for all the gradient and laplacian terms discretization. Known for its stability, the Euler implicit first order bounded time scheme was applied for the temporal terms discretization.

Mesh sensitivity analysis have been conducted for several mesh sizes from 0.3 to 3 million cells. The mesh sensitivity analysis resulted in an adopted mesh of size of 2.16 millions cells. The mesh independent results were verified based on local patterns of the local volume fraction at the points A, B, C (negligible variations).

All 3D simulations were conducted over 32 central processing units (intel CPUs) on a private cluster (each CPU of 2.3 GHz).

The time step was set 10^{-4} *sec*. respecting the condition of numerical diffusion stability through the CourantFriedrichsLewy law such that $CFL < 1$. This time step was selected after time-step adjustments according to the CFL condition in order to ensure time-step independent results. The total physical time of a simulation is 4 *sec*..

Convergence had been assured by looking to all the residuals achieving very low values $\sim O(10^{-6})$ (For example see figure 5-b). Attention, the jumps in the residuals are normal and they are due to the two loops inner/outer of the PIMPLE algorithm applied in OpenFOAM using the mixture model.

For post-processing, three times were considered: 400 *ms*, 800 *ms* and 2500 *ms* where *ms* stands for milliseconds.

4. Results and discussions

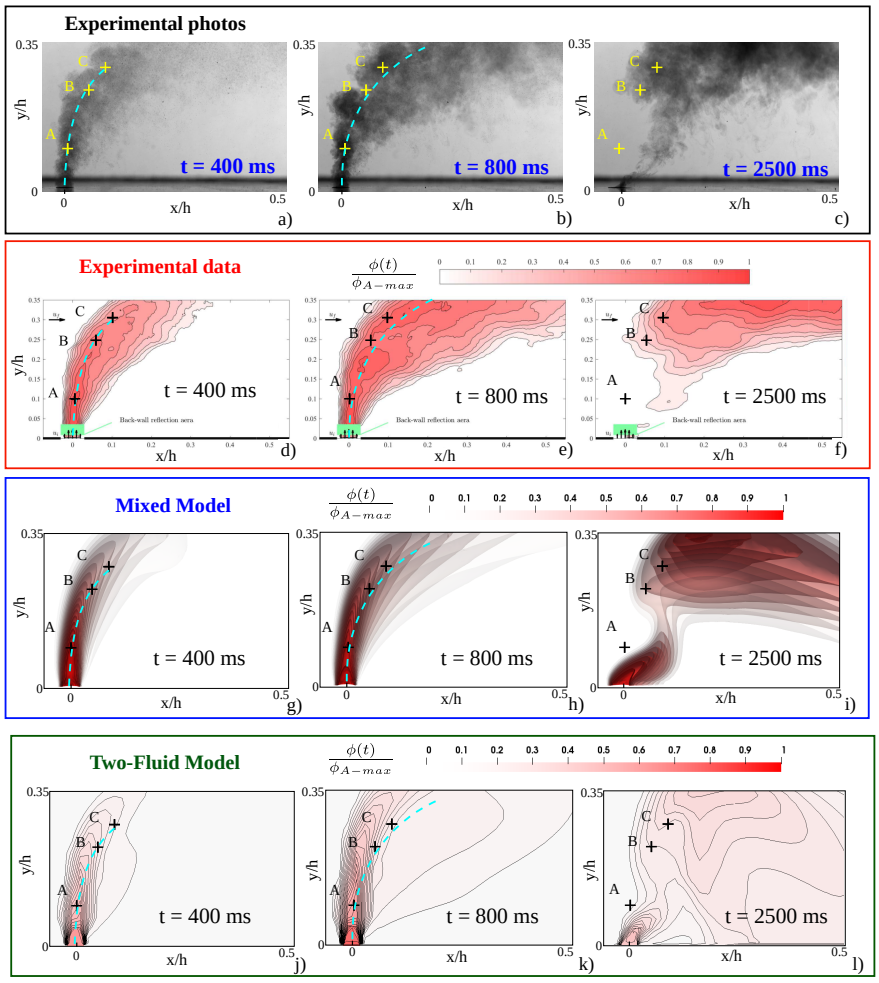

Figure 6: Experimental and numerical normalized concentration fields at t=400, 800 and 2500 ms. a-f) experimental results; g-i) numerical results at $z = 0$ applying the mixture model new solver in OpenFOAM; j-l) numerical results at $z = 0$ applying the two-fluid model in Star-CCM+ with drag model parameters $n = -1.65$, $l_{cd} = 20\ m$.

Using the new solver mixture model developed in OpenFOAM (for a total physical time of 4 seconds), the solution required 22.08 hours as computational time, solved in OpenFOAM in parallel on a cluster of 32 intel processors (each 2.3 GHz).

The new solver via the mixture model in OpenFOAM required a computational time that is less by a factor of the order of O(~10), compared to the commercial two-fluid model in Star-CCM+.

The concentration profiles for the liquid-solid jet's bend are shown in figure 6. It can be clearly observed that the numerical results are very close to the experimental

data at the different times 400, 800 and 2500 ms. The new solver developed in OpenFOAM as a mixture model predicted slightly-better the jet's bend or jet's trajectory at $t = 400$ *ms* and $t = 800$ *ms* compared to the two-fluid model as shown from the iso-surface contour-lines of figures 6-(g,h). Moreover, at $t = 2500$ *ms* the mixture model predicted a fairly accepted particles concentration contour map as can be seen in figure 6-(i). More precisely, looking to the experimental data at $t = 2500$ *ms* of figure 6-(f), the mixture model succeeded to predict the absence of particles in the region $(x/h > 0.2;\ y/h < 0.15)$ as it can be seen from figure 6-(i). However, at the same time $t = 2500$ *ms*, the two-fluid model failed to predict the absence of particles in the region $(x/h > 0.2;\ y/h < 0.15)$ (see figure 6-(l)).

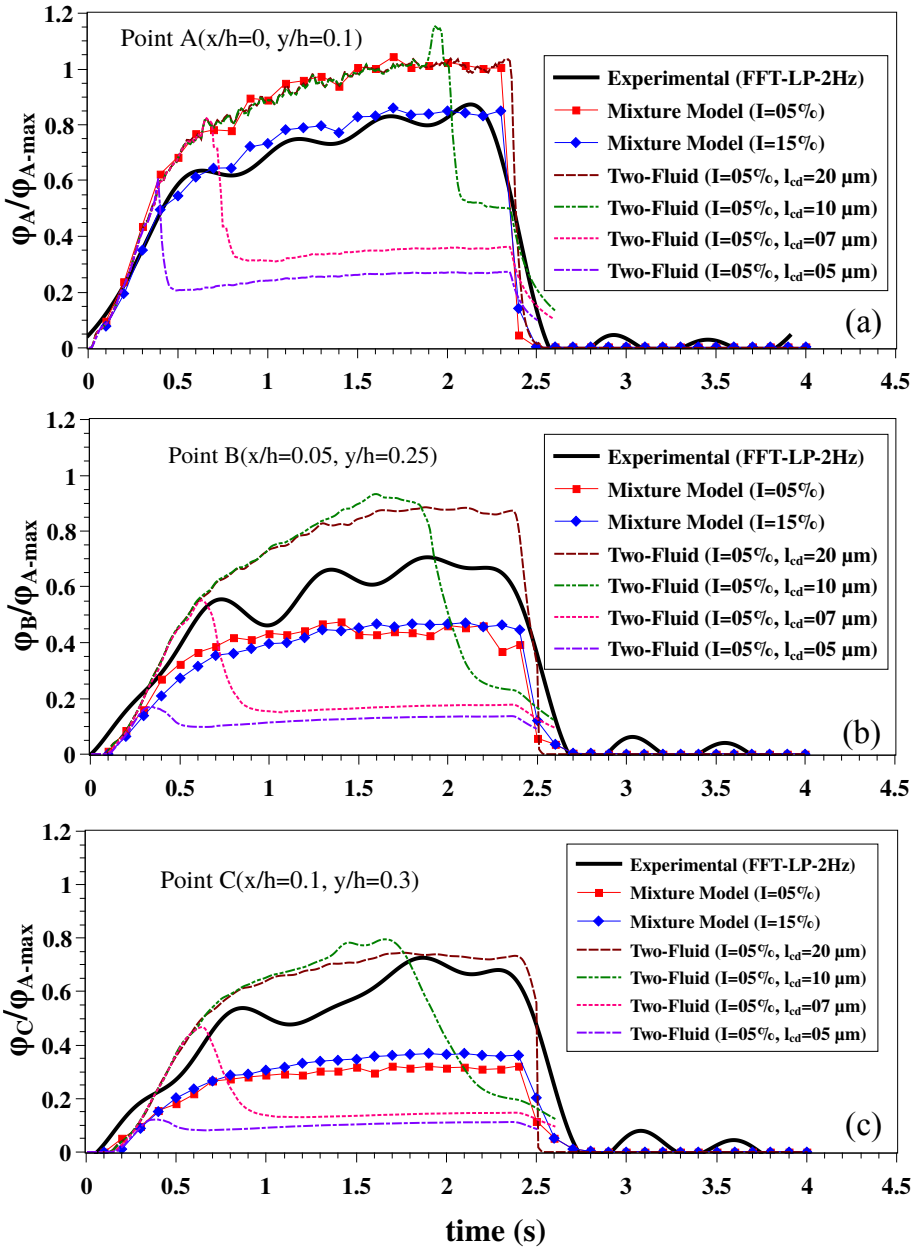

Figure 7: The normalized particle's concentration values of the spatially averaged line probes located at the points A($x/h = 0$, $y/h = 0.1$), B($x/h = 0.05$, $y/h = 0.25$) and C($x/h = 0.1$, $y/h = 0.3$) as function of time. $\phi_{A-max} \approx 5.7\%$ corresponds to the maximum value obtained at the point A between t=0 and t=4 s. The l_{cd} parameter corresponds to the term in the drag coefficient model of equation 21.

For deeper local analysis near the jet's entry, three points of the experimental concentration field located at the jet's bend were considered: A ($x/h = 0$, $y/h = 0.1$), B ($x/h = 0.05$, $y/h = 0.25$) and C ($x/h = 0.1$, $y/h = 0.3$). These three points correspond to local line probes positions that have been considered at each point (A, B, and C) rather than only single points. This is in order to do an averaging of the concentration values in the direction perpendicular to the plane of visualization by the camera. Moreover, all the real experimental data were then filtered by applying a low-pass filter (FFT-LP) of a cut-off frequency of 2 Hz.

The normalized local concentration values located at these points A, B and C are plotted as function of time as shown in figure 7.

At the point A(x/h=0, y/h=0.1) of figure 7-a: using a turbulence intensity of about $I = 5\%$, both the two-fluid and mixture models slightly overestimated the particles volume fraction compared to experimental data. The mixture model approaches the experimental data at a turbulence intensity I of about 15%. The effect of modifying I between 5% and 15% on the particles volume fraction was negligible while employing the two-fluid model in star-CCM+ at the points A, C and B (investigated at $l_{cd} = 20\ \mu m$).

At the point B(x/h=0.05, y/h=0.25) of figure 7-b: the mixture model is found to predict in general a closer CFD results to the experimental data than the two-fluid model, especially between 0 and 1.5 seconds. At higher values of the interaction length scale parameter of the drag coefficient model of eqn. 21, the two-fluid model overestimated the volume fraction of particles between for all $t > 0.7$ seconds. However, it can be seen that decreasing the value of l_{cd} (in other words increasing the value of C_D coefficeint of eqn. 22), the two-fluid model predicts lower concentration values with a modified critical time. Moreover, the same figure 7-b shows that increasing I value in the mixture model from 5% to 15% results in a slight change in the normalized volume fraction $\frac{\phi_B}{\phi_{A-max}}$. This latter influence of I was observed to be limited only to the mixture model.

At the point C(x/h=0.1, y/h=0.3) of figure 7-c, for $t < 1$ and $t > 1.4$ seconds, the two-fluid model predicted ϕ_C values that are more close to the experimental data than the mixture model. However the mixture model predicted closer ϕ_C values for $1 \leq t \leq 1.4$ seconds.

The primary conclusion that can be made from figures 6 and 7 is that the two-fluid model can be applied for predicting suspension JICF, but it requires *a huge amount of time* in order to better quantify its sensitivity to the numerous model parameters. However the mixture model in nature includes less number of equations to be solved, and less number of parameters thus it constitutes a very good compromise in terms of accepted accuracy versus computational time.

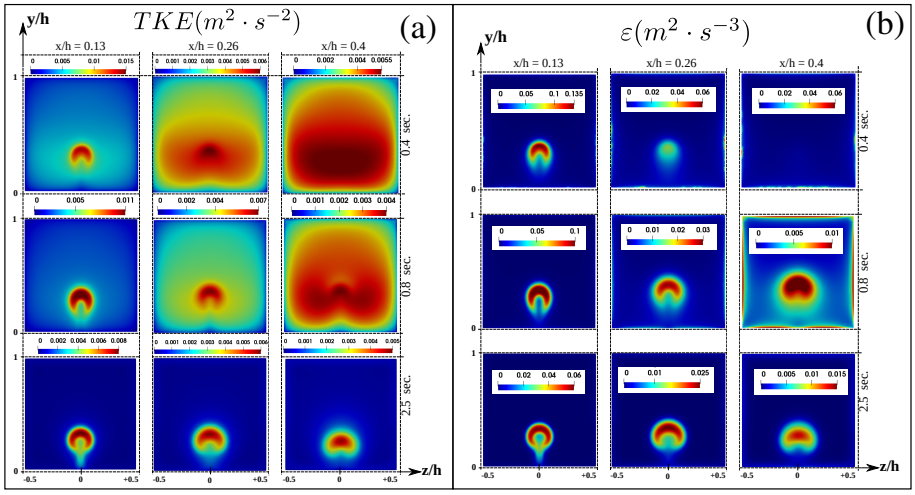

Figure 8: (a) The turbulent kinetic energy (TKE), and (b) the turbulence dissipation rate (ε) at different cross section planes, using the mixture model new solver in OpenFOAM.

The turbulent kinetic energy (TKE) at different cross section planes perpendicular to the jet flow is illustrated in figure 8-a for the mixture model new solver in OpenFOAM. The vortical structures of a jet in a crossflow can be clearly observed as know in the literature (see figure 1).

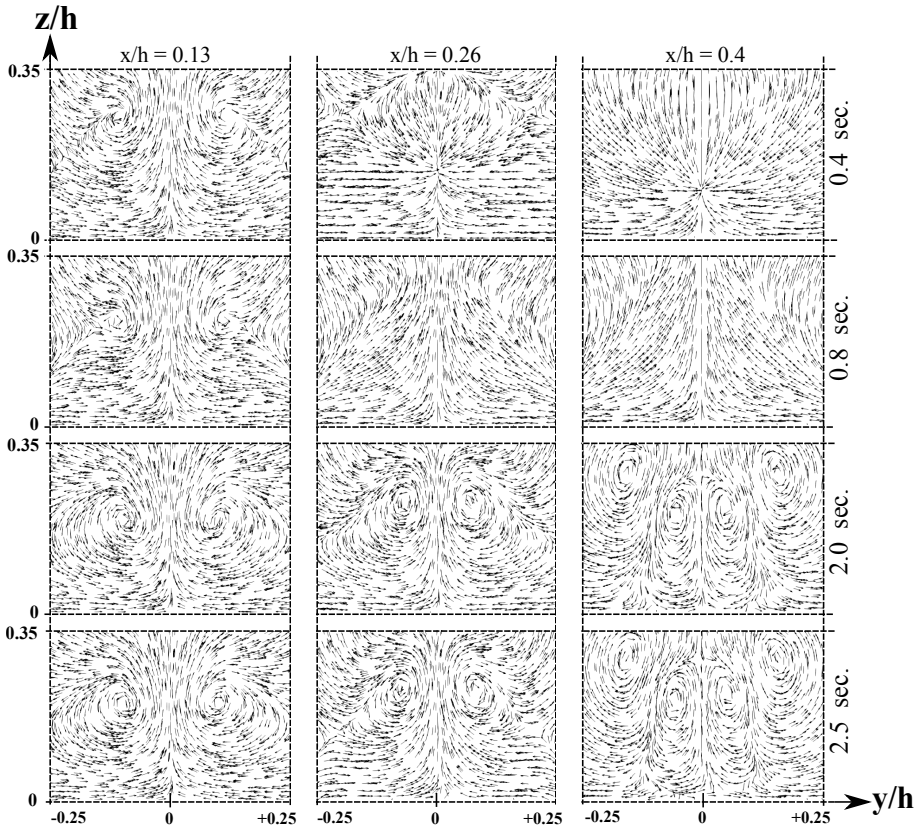

Figure 9: The velocity streamlines at different planes inside the channel, using the mixture model.

Figure 9 shows the several vortex structures such as the leading edge and lee-side vortices along the jet, the horseshoe vortex system, wake vortices and counter-rotating vortex pair. This is in coherence with the theory shown in figure 1-a. At early injection, the vortex system contains the highest TKE that is then dissipated with time due to energy dissipation while jet penetrates the cross flow. This is also confirmed by looking to the turbulence dissipation rate values which are presented in figure 8-b.

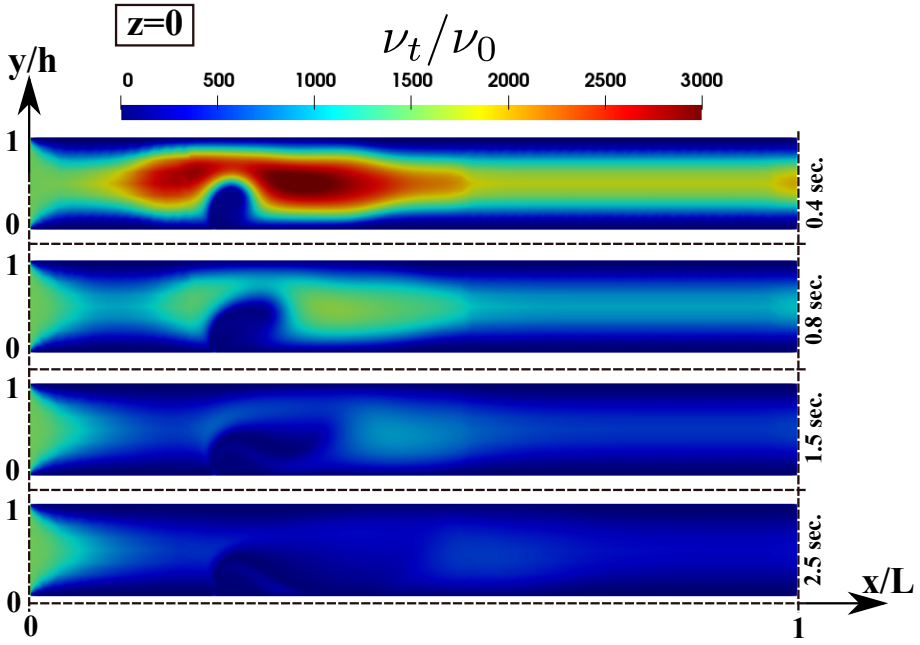

Figure 10: The dimensionless turbulent viscosity as function of time inside the channel, at the central plane $z = 0$, using the mixture model new solver in OpenFOAM.

The variation of the dimensionless turbulent viscosity ν_t/ν_0 as function of time, inside the channel at the central plane $z = 0$, is shown in figure 10. It can be clearly observed that the turbulent viscosity, at the central xy-plane $z = 0$, decreases with time due to the vortex structure evolution, and the stopping of particles injection at $t = 2.5\ s$.

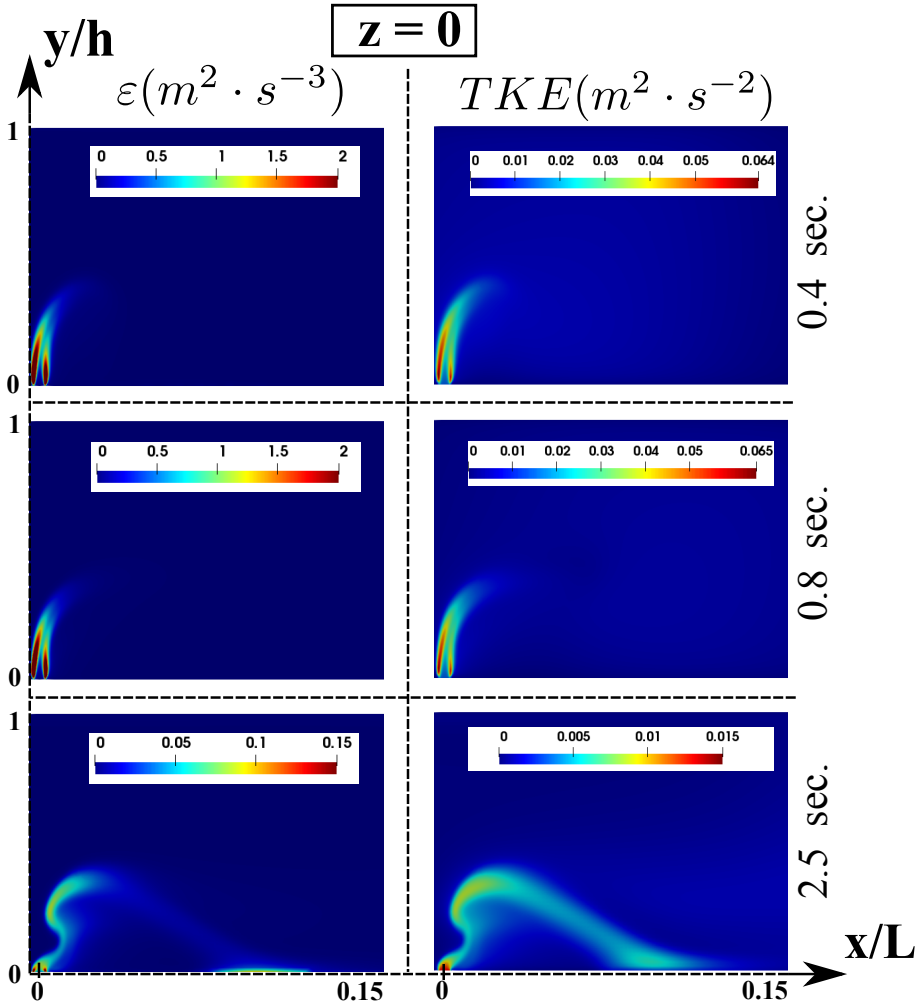

Figure 11: The dimensionless turbulent viscosity as function of time inside the channel, at the central plane $z = 0$, using the mixture model new solver in OpenFOAM.

Both the turbulence dissipation and the TKE as function of time, inside the channel at the central plane $z = 0$, are shown in figure 11. It can be observed that energy dissipation increases near the jet's inlet and along the cross flow.

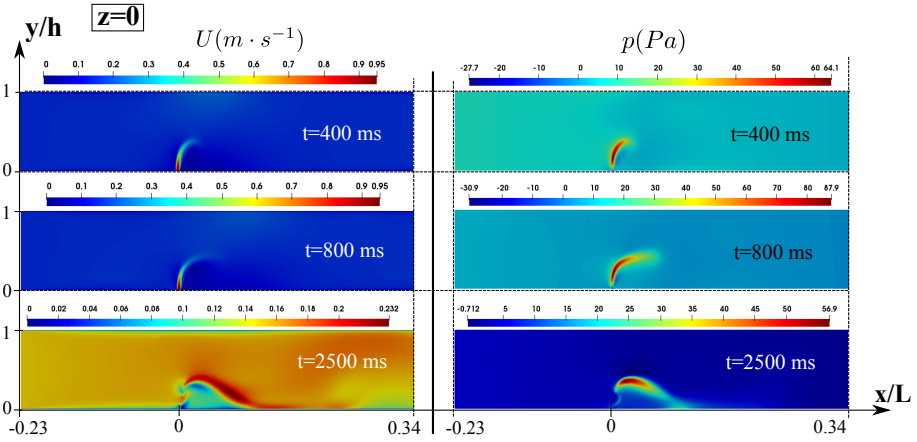

Figure 12: The velocity and the pressure fields, at the central plane $z = 0$, using the mixture model new solver in OpenFOAM.

Figure 12 shows the local velocity magnitude and the pressure fields as function of time, at the central plane $z = 0$ predicted by new solver mixture model in OpenFOAM.

5. Conclusion and perspectives

A vertical upward liquid-solid two-phase jet in crossflow (JICF, of density ratio $\rho_p/\rho_f = 10.3$) has been investigated, both experimentally (via camera and image tracking technique) and numerically (via two approaches: a *Two-Fluid* model with a modified $k-\varepsilon$ turbulence model, and a *Mixed* model, as a new CFD solver developed in OpenFOAM, with a buoyant $k-\varepsilon$ turbulence model). The total period of the experiment and CFD simulations is very short and equals to 4 seconds.

At different times, in the zone close to the jet's entry $(x/h \leq 0.1,\ y/h \leq 0.3)$ both models predicted local particles volume fraction values that were fairly close to the experimentally measured ones at 3 points A(x/h=0,y/h=0.1), A(x/h=0.05,y/h=0.25)and C(x/h=0.1,y/h=0.3). Moreover, the developed mixture model, predicted well the liquid-solid jet's bend and the particles concentration map at the time $t = 2500\ s$ with particles absence in the zone $(x/h > 0.2;\ y/h < 0.15)$. The two-fluid model predicted particles presence in the latter zone which was not observed experimentally. Thus the mixture model constitutes a good compromise for conducting global analysis of suspension JICFs due to its acceptable accuracy associated with a computational cost that is reduced by a factor of the order of O(~10).

Future investigations are still necessary, both experimentally and numerically (e.g. a larger interval of drag coefficient model parameters), in order to enhance the qualitative predictions of the Euler-Euler Multiphase models, by extrapolating the physics from the microscopic scale to the macroscopic one (e.g. from DEM-CFD coupling approach including 4-way coupling in order to have more complete modeling approach that accounts for different ratios of the particle response time τ_p to the Kolmogorov time scale τ_K as illustrated in figure 1 by Elghobashi in 1994 [26]).

Finally, further studies are expected both numerically and experimentally in order to explore the influence of the particles' size distribution (or polydispersity), the particles maximum load concentration (at inlet), and the particles to fluid density ratio in liquid-solid two-phase JICF. This will be in attempts to explore the limits of the Euler-Euler modeling approaches when simulating liquid-solid jets in turbulent liquid crossflow.

Acknowledgment

This work was carried out within the framework of Research on Ground Transports and Mobility by the French National Scientific Research Center CNRS, in coordination with the ELSAT2020 project supported and financed by the European Community, the French Ministry of Higher Education and Research, the Hauts-de-France Regional Council. The authors gratefully acknowledge and appreciate the support of all these institutions. It was also supported by ALSTOM SA, which funds a part of the present research work.

References

[1] Andreopoulos J, Rodi W. Experimental investigation of jets in a cross flow. Journal of Fluid Mechanics, 1984, 138: 93–127.

[2] Muppidi S, Mahesh k. Study of trajectories of jets in crossflow using direct numerical simulations. Journal of Fluid Mechanics, 2005, 530: 81–100.

[3] New T, Lim T, Luo S, A flow field study of an elliptic jet in cross flow using piv technique. Experiments in Fluids, 2004, 36: 604–618.

[4] Pathak M, Dass A, Dewan A. An investigation of turbulent rectangular jet discharged into a narrow channel weak crossflow. Journal of Hydrodynamics 2008, 20(1): 154–163.

[5] Smith S, Mungal M, structure and scaling of the jet in crossflow. Journal of Fluid Mechanics, 1998, 357: 83–122.

[6] Guo T-T, Li S-H, Xu Z. Numerical simulation of turbulent jets with lateral injection into a crossflow. Journal of Hydrodynamics, 2006, Ser. B, 18(3):319–323.

[7] Xiao Y, Wang H-W. Numerical study of hydrodynamics of multiple tandem jets in cross flow. Journal of Hydrodynamics, 2011, 23(6): 806–813.

[8] Forney LJ, Feng Z and Wang X. Jet Trajectories of Transverse Mixers at Arbitrary Angle in Turbulent Tube Flow. Chemical Engineering Research and Design, 1999, 77(8), 754-758.

[9] Torr JP, Fletcher DF, Touche I, Lasuye T and Xuereb C. Jet injection studies for partially baffled mixing reactors: A general correlation for the jet trajectory and jet penetration depth. Chemical Engineering Research and Design, 2008, 86, 11171127.

[10] Torr, JP, Fletche DF, Lasuye T and Xuereb C. An experimental and CFD study of liquid jet injection into a partially-baffled mixing vessel: a contribution to process safety by improving the quenching of runaway reactions. Chem. Eng. Sci., 2008, 63(4): 924942.

[11] Margason R. Fifty years of jet in cross flow research. AGARD Symposium on a Jet Cross Flow, Inchester, UK, 1993, CP-534.

[12] Lai A, Lee J. Multiple tandem jet interaction in a crossflow. Journal of Hydrodynamics, 2010, 22(5): 639–643.

[13] Fan J, Xu S-L, Wang D-Z. PDA measurements of two-phase flow structure and particle dispersion for a particle laden jet in crossflow. Journal of Hydrodynamics, 2010, 22(1): 9–18.

[14] Kasat GR, Khopkar AR, Ranade VV, Pandit AB. CFD simulation of liquid-phase mixing in solid-liquid stirred reactor. Chemical Engineering Science, 2008, 63(15): 3877-3885.

[15] White C. A study of heat transfer to liquid-solid suspensions flowing turbulently in a horizontal pipe. A PhD Thesis,1955, Georgia Institute of Technology.

[16] Guazzelli E, Morris J. A Physical Introduction to Suspension Dynamics (Cambridge Texts in Applied Mathematics), 2011, Cambridge University Press.

[17] Guazzelli E. Rheology of dense suspensions of non colloidal particles. Powders and Grains. EPJ Web of Conferences, 2017, 140: 01001.

[18] Leighton D, Acrivos A. Measurement of self-diffusion in concentrated suspensions of spheres. Journal of Fluid Mechanics, 1987, 177: 109–131.

[19] Leighton D, Acrivos A. The shear-induced migration of particles in concentrated suspensions, Journal of Fluid Mechanics, 1987, 181: 415–439.

[20] Gadala-Maria F, Acrivos A. Shear-induced structure in a concentrated suspension of solid spheres. Journal of Rheology, 1980, 24: 799.

[21] Chapman B. Shear-induced migration phenomena in concentrated suspensions. Ph.D. thesis, 1990, University of Notre Dame, Indiana, USA.

[22] Dbouk T, Lobry L, Lemaire E, Moukalled F. Shear-induced particles migration: predictions from experimental determination of the particle stress tensor. Journal of Non-Newtonian Fluid Mechanics, 2013, 198: 78–95.

[23] Gallier S, Lemaire E, Lobry L, Peters F. Effect of confinement in wall-bounded non-colloidal suspensions. Journal of Fluid Mechanics, 2016, 799: 100–127.

[24] Miller R, Singh J, Morris J. Suspension flow modeling for general geometries. Chem. Eng. Sci. 2009, 64: 4597–4610.

[25] Dbouk T. A suspension balance direct-forcing immersed boundary model for wet granular flows over obstacles. Journal of Non-Newtonian Fluid Mechanics, 2016, 230: 68–79.

[26] Elghobashi S. On predicting particle-laden turbulent flows. Applied Scientific Research, 1994, 52: 309–329.

[27] Yeoh G, Tu J. Computational Techniques for Multi-Phase Flows. Elsevier, 2010, ISBN: 9780080467337.

[28] Derksen J.J., Numerical simulation of solids suspension in a stirred tank, AIChEJournal 49, 11, 2003, 27002714.

[29] Blais B, Lassaigne M, Goniva C, Fradette L, Bertrand F. Development of an unresolved CFD-DEM model for the flow of viscous suspensions and its application to solid-liquid mixing. Journal of Computational Physics, 2016, 318: 201–221.

[30] Cierco F-X, Naaim M, Naaim-Bouvet F. Experimental study of particle concentration fluctuations in a turbulent steady flow. Annals of Glaciology, 2008, 49.

[31] Fric T.F., Roshko A. Vortical structure in the wake of a transversejet, J. of Fluid Mech., 1994, 279: 1-47.

[32] Brennen CE. Fundamentals of Multiphase Flow. Cambridge University Press, 2005, ISBN: 9780511807169.

[33] Ishii M, Hibiki T. Thermo-Fluid Dynamics of Two-Phase Flow. Springer, 2011, ISBN: 9781441979858.

[34] Takacs I, Patry G, Nolasco D. A dynamic model of the clarification-thickening process. Water Res. 1991, 25(10): 1263–1271.

[35] Dbouk T, Lobry L, Lemaire E. Normal stresses in concentrated non-brownian suspensions. Journal of Fluid Mechanics, 2013, 715: 239–272.

[36] Henkes R, Vlugt FVD, Hoogendoorn C. Natural convection flow in a square cavity calculated with low-reynolds-number turbulence models. Int. J. Heat Mass Transfer, 1991, 34: 1543–1557.

[37] Nicolette V, Tieszen S, Black A, Domino S, O'Hern T. A turbulence model for buoyant flows based on vorticity generation. Sandia Nationl Laboratory, 2005, Sandia Report 6273.

[38] Wilcox D. Turbulence modeling for CFD, Third Edition. Birmingham Press, Inc.,California, 2006, ISBN 978-1928729082.

[39] Gidaspow D. Hydrodynamics of fluidization and heat transfer: Supercomputer modeling. Appl. Mech. Rev. 1996, 39.

[40] Bouillard J, Lyczkowski R, Gidaspow D. Porosity distributions in a fluidized bed with an immersed obstacle. AIChE 1989, 35: 908–922.

[41] Wen C, Yu Y. Mechanics of fluidization. Chem. Eng. Prog. Symp. Ser.1966, 62: 100–111.

[42] Schiller L, Naumann A. Uber die grundlegenden berechnungen bei der schwerkraftaufbereitung. VDI Zeits 1933, 77(12): 318–320.

[43] Richardson J, Zaki W. Sedimentation and fluidization:part i, Trans. Inst. Chem. Eng. 1954, 32: 35–47.

[44] Greifzu F, Kratzsch C, Forgber T, Lindner F, Schwarze R. Assessment of particle-tracking models for dispersed particle-laden flows implemented in openfoam and ansys fluent. Engineering Applications of Computational Fluid Mechanics, 2016, 10(1): 30–43.

[45] Thai-Van D, Minier J, Simonin O, Freydier P, Olive J. Multidimensional two fluid model computation of turbulent dispersed two phase flows. ASME FED, 1994, 185: 177–291.

[46] Simonin O. Prediction of the dispersed phase turbulence in particle-laden jets, gas-solid flows. ASME FED, 1991, 121: 197–206.

[47] Hinze J. Turbulence. McGraw-Hill, 1975, ISBN: 978-0070290372.

[48] Shih T. Liou W, Shabir A, Zhu J. A new k-e eddy-viscosity model for high reynolds numner turbulent flows: a model development and validation. Computers Fluids, 1991, 24: 227–238.

[49] Rodi W. Experience with two-layer models combining the k-e model with a one-equation model near the wall. AIAA, 1991, 91: 02–16.

[50] Launder B. Spalding D. The numerical computation of turbulent flows. Computer Methods in Applied Mechanics and Engineering, 1974, 3(2): 269–289.

Appendix

Two-Fluid approach: turbulence modeling

Following the RANS approach, any instantaneous field term represented by ξ is decomposed as a steady mean term $\bar{\xi}$ and a fluctuating term ξ' according to: $\left[\xi = \bar{\xi} + \xi'\right]$. For the continuous phase, two transport equations two-layers-realizable-$(k-\varepsilon)$ turbulence model [48] is solved for the turbulent kinetic energy k and the turbulent dissipation rate ε as it will be shown in details in the next section.

For any continuous phase i, two modified transport equations are solved for the turbulence kinetic energy k_i and dissipation rate ε_i by applying a modified-realizable-$(k-\varepsilon)$ turbulence model with two-layers approach [48]. The modifications with respect to the original $(k-\varepsilon)$ turbulence model include the volume fractions of each phase, and additional source terms that account for the effect of the dispersed phase on the continuous phase turbulence field. The two-layer approach, first suggested by Rodi [49], is an alternative to the low-Reynolds number approach which allows the $(k-\varepsilon)$ model to be applied in the viscous-affected layer such that in the layer next to the wall, the turbulent dissipation rate and the turbulent viscosity are specified as functions of wall distance. The two-layers modified-realizable-$(k-\varepsilon)$ turbulence model [27] is given as the following:

$$\begin{aligned}\frac{\partial\left(\phi_i\rho_i k_i\right)}{\partial t}+\nabla\cdot\left(\phi_i\rho_i k_i\bar{\mathbf{U}}_i\right) &= \nabla\cdot\left[\phi_i\left(\mu_i+\frac{\mu_i^t}{\sigma_k}\right)\nabla k_i\right]\\ &+\phi_i\left(P_i+G_i-\rho_i\varepsilon_i\right)+S_{\varepsilon,c,PIT}+\sum_{i\neq j}\phi S_{\varepsilon,ij}\end{aligned} \tag{34}$$

$$\begin{aligned}\frac{\partial\left(\phi_i\rho_i\varepsilon_i\right)}{\partial t}+\nabla\cdot\left(\phi_i\rho_i\varepsilon_i\bar{\mathbf{U}}_i\right) &= \nabla\cdot\left[\phi_i\left(\mu_i+\frac{\mu_i^t}{\sigma_\varepsilon}\right)\nabla\varepsilon_i\right]\\ &+\phi_i\frac{\varepsilon_i}{k_i}\left(C_{\varepsilon 1}P_i+|G_i|-C_{\varepsilon 2}\rho_i\varepsilon_i\right)+S_{\varepsilon,c,PIT}+\sum_{i\neq j}\phi S_{\varepsilon,ij}\end{aligned} \tag{35}$$

σ is the turbulent Prandtl number, μ the dynamic viscosity, $\bar{\mathbf{U}}$ the mean velocity, P the production term and G is the dissipation term given, respectively by:

$$P_i = \mu_i^t \nabla \mathbf{U}_i \cdot \left[\nabla \mathbf{U}_i + (\nabla \mathbf{U}_i)^T\right] - \frac{2}{3}\nabla \cdot \mathbf{U}_i \left(\mu_i^t \nabla \cdot \mathbf{U}_i - \rho_i \mathbf{U}_i\right) \tag{36}$$

$$G_i = -\frac{\mu_i^t}{\rho_i}\mathbf{g} \cdot \nabla \rho_i \tag{37}$$

$\mu_i^t \equiv \mu_c^t$ is the turbulent dynamic viscosity of a continuous phase i computed as the following:

$$\mu_i^t = \rho_i C_\mu f_\mu \frac{k_i^2}{\varepsilon_i} \tag{38}$$

The turbulence of the dispersed phase is correlated to that of the continuous phase by introducing a response function C_t that will be detailed in the next section.

f_μ is a damping function that enforces realizability and mimic the decrease of turbulent mixing near the walls for turbulence models that resolve the viscous- and buffer-layer. It is usually set to unity in the original $(k-\varepsilon)$ model, but in the present modified model it is modeled as a function of the flow properties such as the wall-distance, turbulent and Kolmogorov Reynolds numbers [49].

The modified-$(k-\varepsilon)$ turbulence model coefficients based on [50] were applied as the following:

$$C_\mu = 0.09, \;\; \sigma_k = 1.0; \;\; \sigma_\varepsilon = 1.3; \;\; C_{\varepsilon 1} = 1.44; \;\; C_{\varepsilon 2} = 1.92 \tag{39}$$

Two-Fluid approach: Dispersed phase turbulence

For the dispersed phase, the turbulence is correlated to the continuous phase turbulence by using semi-empirical models introduced as additional source terms in the $(k-\varepsilon)$ model. The correlations are given by a response function C_t that is defined as the ratio of the dispersed phase velocity fluctuation to that of the continuous phase such that:

$$k_d = C_t^2 k_c \tag{40}$$

$$\mu_d^t = \frac{\rho_d}{\rho_c} C_t^2 \mu_c^t \tag{41}$$

$$C_t = \left|\frac{\mathbf{U'}_d}{\mathbf{U'}_c}\right| \tag{42}$$

Where $\mathbf{U'}_d$ is the velocity fluctuation of the dispersed phase and $\mathbf{U'}_c$ is that of the continuous phase.

Turbulence Interaction: Particle Induced Turbulence (PIT)

The influence of the dispersed phase on the turbulence of the continuous phase is taken into account through the $S_{k,c,PIT}$ and $S_{\varepsilon,c,PIT}$ source terms thus considering Par-

ticle Induced Turbulence (PIT). Following the Tchen's theory of dispersion of discrete particles by homogeneous turbulence [47, 45, 46], it is given as the following:

$$S_{k,c,PIT} \;=\; C_0 A_D \left(q_{cd} - 2q_c^2 - \mathbf{U}_{TD} \cdot \mathbf{u}_r \right) \tag{43}$$

q_{cd} and q_c are given, respectively by:

$$q_{cd} \;=\; 2\left(\frac{b+\eta}{1+\eta} \right) k_c \quad , \quad q_c \;=\; \sqrt{k_c} \tag{44}$$

Note that if $\rho_d \gg \rho_c$ (b is small), the transfer term becomes a sink of continuous phase turbulence kinetic energy. If $\rho_d \ll \rho_c$ (b tends to $\frac{3}{2}$) and if $C_{VM} = \frac{1}{2}$, then the transfer term becomes a source of continuous phase turbulence kinetic energy.